

**MACHINE LEARNING APPROACH TO PREDICT STRESS IN  
CERAMIC/EPOXY COMPOSITES USING MICRO-MECHANICAL  
RAMAN SPECTROSCOPY**

by

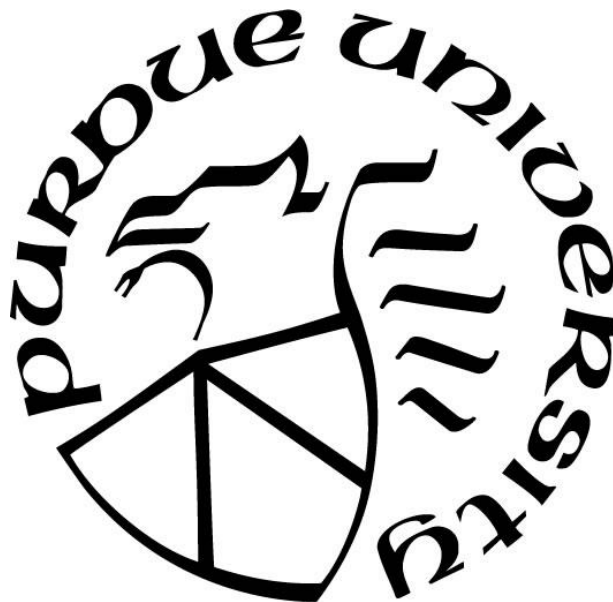
**Abhijeet Dhiman**

**A Thesis**

*Submitted to the Faculty of Purdue University*

*In Partial Fulfillment of the Requirements for the degree of*

**Master of Science**



School of Aeronautics and Astronautics

West Lafayette, Indiana

December 2018

**THE PURDUE UNIVERSITY GRADUATE SCHOOL  
STATEMENT OF COMMITTEE APPROVAL**

Dr. Vikas Tomar, Chair

School of Aeronautics and Astronautics

Dr. Weinong Chen

School of Aeronautics and Astronautics

Dr. Tyler Tallman

School of Aeronautics and Astronautics

**Approved by:**

Dr. Weinong Chen

Head of the Graduate Program

*I dedicate this dissertation to my parents for instilling the importance of hard work and for supporting me pursuing my master degree.*

## **ACKNOWLEDGMENTS**

I am greatly appreciative to Prof. Vikas Tomar whose encouragement, supervision and support from the preliminary to the concluding level enabled me to complete my study. This thesis would not have been possible without his support. I would also like to thank Prof. Tyler Tallman and his students Hashim Hassan, Julio Hernandez, Goon mo Koo and Akshay Jacob Thomas. I thank them for their helpful suggestions, insightful discussions and their good-natured support. I would also like to thank Chandra Prakash and other fellow graduate students who supported me in any respect during the completion of the project.

## TABLE OF CONTENTS

LIST OF TABLES .....	6
LIST OF FIGURES .....	7
LIST OF SYMBOLS .....	9
LIST OF ABBREVIATIONS.....	11
ABSTRACT.....	12
CHAPTER 1. INTRODUCTION .....	13
1.1 Micro-mechanical Raman spectroscopy.....	13
1.2 Nanoindentation setup .....	15
1.3 Machine learning model .....	17
CHAPTER 2. REVIEW OF LITERATURE .....	21
CHAPTER 3. RESEARCH METHODOLOGY.....	23
3.1 Sample preparation .....	23
3.2 Raman Spectroscopy.....	24
3.3 Micro-mechanical Raman spectroscopy.....	25
3.4 Material characterization .....	27
CHAPTER 4. RESULTS.....	29
4.1 Material characterization .....	29
4.2 Micro-mechanical Raman spectroscopy.....	33
4.3 Finite element method.....	35
4.4 Machine learning algorithm.....	45
CHAPTER 5. SUMMARY, CONCLUSIONS, AND RECOMMENDATIONS.....	50
LIST OF REFERENCES.....	52
PUBLICATIONS.....	55

## LIST OF TABLES

Table 4.1 Constitutive model parameters for epoxy resin matrix.....	32
Table 4.2 Constitutive model parameters for composite .....	32
Table 4.3 Variable used for parametric simulation.....	40

## LIST OF FIGURES

Figure 1.1 Micro-mechanical Raman spectroscopy setup .....	15
Figure 1.2 (A) Nanoindentation platform (Micro Materials Ltd., UK), (B) Schematic diagram of the nanoindentation platform .....	16
Figure 1.3 Different size and orientation of particles inside epoxy resin matrix.....	17
Figure 1.4 Schematic of elliptical particle inside stretched matrix.....	18
Figure 1.5 Schematic of artificial neural network .....	19
Figure 1.6 Schematic of a neuron .....	20
Figure 3.1 Bending test sample.....	23
Figure 3.2 Stress distribution using finite element method .....	24
Figure 3.3 Raman spectrum for strontium titanate particles, epoxy resin system and composite	25
Figure 3.4 Raman spectrum for C-H bond stretching in epoxy resin .....	26
Figure 3.5 Bending Test Sample.....	27
Figure 4.1 Indentation load vs depth for epoxy resin and strontium titanate epoxy composite. ..	29
Figure 4.2 Indentation stress-strain curve for epoxy resin and strontium titanate epoxy composite .....	31
Figure 4.3 Change in Raman shift for epoxy resin with compressive stress. ....	33
Figure 4.4 Stress (tensile) distribution around notch using micro-mechanical Raman spectroscopy.....	34
Figure 4.5 Stress (Tensile) distribution around strontium titanate particle .....	35
Figure 4.6 A) Mesh for beam under uniaxial tension. B) Comparison of results from the FEM model and experiments .....	36
Figure 4.7 Mesh for particle inside epoxy resin matrix. ....	37

Figure 4.8 A) Schematic of elliptical particle inside epoxy resin matrix B) Convergence of model with the number of elements..... 38

Figure 4.9 Stress distribution around elliptical particle from FEM..... 38

Figure 4.10 Validation of FEM results with experimental results..... 39

Figure 4.11 Schematic of particle inside epoxy resin matrix..... 40

Figure 4.12 Variation of stress concentration with the orientation of major axis of the particle with principle stress direction. .... 41

Figure 4.13 Variation of stress concentration factor with A)  $\theta$  B)  $\sigma_{vm}$  and  $r$  C)  $l/b$ ..... 43

Figure 4.14 Log mean square error with training ..... 46

Figure 4.15 Prediction of stress concentration factor using machine learning model ..... 47

Figure 4.16 Prediction of stress distribution around the notch for stresses in non-linear elastic domain..... 48

Figure 4.17 A) Mesh generated for 3-point bending specimen. B) Stress distribution obtained from FEM. C) Convergence of FEM model for 3-point bending test..... 49

## LIST OF SYMBOLS

$\sigma$	: Stress
$\sigma_{VM}$	: Von-misses stress
$\sigma_1, \sigma_2$	: Principle stresses
$w_{no\ stress}$	: Raman shift without induced stress
$w_{stress}$	: Raman shift under induced stress
$\lambda$	: Wavelength
$\Delta\omega$	: Change in Raman shift
$E$	: Elastic modulus
$\varepsilon$	: Strain
$\varepsilon_{PEL}$	: Strain at proportional elastic limit
$\varepsilon_Y$	: Strain at yield strength
$A, B, C, n$	: Constants
$\frac{l}{b}$	: Ratio of length of major and minor axis of elliptical particle
$\theta$	: Angle of major axis of elliptical particle with x-axis
$r$	: Ratio of stresses in principle direction
$Z_j^l$	: Neural unit value the $j^{th}$ element of layer $l$
$W_{jk}^l$	: Weight of connection $k$ to the $j^{th}$ element of layer $l$ .
$a_k^{l-1}$	: Output from layer $l - 1$ and input $k$ to the $j^{th}$ element of layer $l$
$b_j^l$	: Bias of $j^{th}$ element of layer $l$ .
$\psi(Z_j^l)$	: Activation function
$P$	: Indentation load
$a_c$	: Contact radius

$h_e$  : Elastic depth  
 $E_t$  : Tangent elastic modulus  
 $S_{ij}$  : Stress concentration factor

## LIST OF ABBREVIATIONS

FEM	: Finite element method
PEL	: Proportionality elastic limit
ANN	: Artificial neural network
ReLU	: Rectified linear units

## ABSTRACT

Author: Dhiman, Abhijeet. MS

Institution: Purdue University

Degree Received: December 2018

Title: Machine Learning Approach to Predict Stress in Ceramic/Epoxy Composites using Micro-Mechanical Raman Spectroscopy

Committee Chair: Vikas Tomar

Micro-mechanical Raman spectroscopy is an excellent tool for direct stress measurements in the structure. The presence of mechanical stress changes the Raman frequency of each Raman modes compared to the Raman frequencies in absence of stress. This difference in Raman frequency is linearly related to stress induced and can be calibrated to stress by uniaxial or biaxial tension/compression experiments. This relationship is not generally linear for non-linear behavior of the materials which limits its use to experimentally study flow stress and plastic deformation behavior of the material. In this work strontium titanate ceramic particles dispersed inside epoxy resin matrix were used to measure stress in epoxy resin matrix with non-linear material behavior around it. The stress concentration factor between stress induced inside ceramic particles and epoxy resin matrix was obtained by non-linear constitutive finite element model. The results of finite element model were used for training a machine learning model to predict stress in epoxy resin matrix based on stress inside ceramic particles. By measuring stress inside ceramic particles using micro-mechanical Raman spectroscopy, the stress inside epoxy matrix was obtained by pre-determined stress concentration factor.

## CHAPTER 1. INTRODUCTION

### 1.1 Micro-mechanical Raman spectroscopy

Micro-mechanical Raman spectroscopy has been developed as an excellent tool for direct stress measurements [1-8] at meso and microscales. Micro-mechanical Raman spectroscopy is a non-contact and non-distractive method which is capable of measuring the stress at micron scale without measuring the strains [1, 2, 5-12]. Raman frequencies are associated with the Rayleigh scattering of photons due to inelastic collisions of the photons with the molecules. Therefore, the Raman shifts signify the change in the energy between the two states. The difference between the Raman frequencies in the presence of stress and in the absence of stress can be directly related to the stress induced in the structure. The relationship between effective stress and change in Raman shift is represented as [1, 2, 5-12]

$$\sigma = C \times \Delta\omega \quad (1)$$

where C is a material constant obtained by uniaxial experiments and  $\Delta\omega$  is the change in Raman shift between stressed and unstressed states, respectively.  $\Delta\omega > 0$  indicates compressive stress and  $\Delta\omega < 0$  indicates tensile stress. While equation (1) can be used to measure stress in the linear elastic domain, the extension of this correlation for the non-linear material behavior is difficult to obtain.

This work presents an innovative technique to measure stress in the non-linear elastic domain in the case of a ceramic-epoxy composite. The stress state in the epoxy resin system was obtained in the non-linear elastic domain by introducing strontium titanate particles of a size smaller than 5  $\mu\text{m}$  inside epoxy resin matrix. During loading the load is chosen that while the

stresses induced inside epoxy resin matrix are in the non-linear elastic domain, the stresses induced inside ceramic particles are in linear elastic domain due to the comparatively large elastic modulus. The stresses induced inside the titanate particle due to matrix deformations is a function of several parameters such as particle geometry, particle orientation, and distance from the free surface, interface mechanics. In this work, the effects of particle geometry and particle orientation were studied by parametric evaluation of a finite element method (FEM) model that simulates a single particle inside infinite isotropic epoxy resin matrix. This model assumes an ideal interface between the epoxy resin matrix and the ceramic particle under static equilibrium. Since the non-linear deformation in epoxy resin system is recoverable till yield stress, a model similar to multi-linear elastic model was used for constitutive description as:

$$\sigma = \begin{cases} E\varepsilon & \varepsilon < \varepsilon_{PEL} \\ A\varepsilon^n + B & \varepsilon_{PEL} \leq \varepsilon < \varepsilon_Y \end{cases} \quad (2)$$

where  $\varepsilon_{PEL}$  is strain at proportionality elastic limit (PEL) and  $\varepsilon_Y$  is strain at yield point. E is the elastic constant of material for linear elastic behavior till proportionality elastic limit. Beyond proportionality elastic limit, the material shows non-linear transition to yield point. The multilinear elastic model for nonlinear elastic behavior was replaced with power law for continuous measurement of tangent stiffness. A, B and n are constants obtained by fitting the constitutive model to experimental data.

The apparatus used in this work consists of a Raman microscope from HORIBA scientific and a mechanical loading stage from Deben UK Ltd. with a maximum load capacity of 2 kN. The experiment setup shown in Figure 1.1 has a Raman microscope coupled with loading stage to obtain stress distribution as a function of applied load.

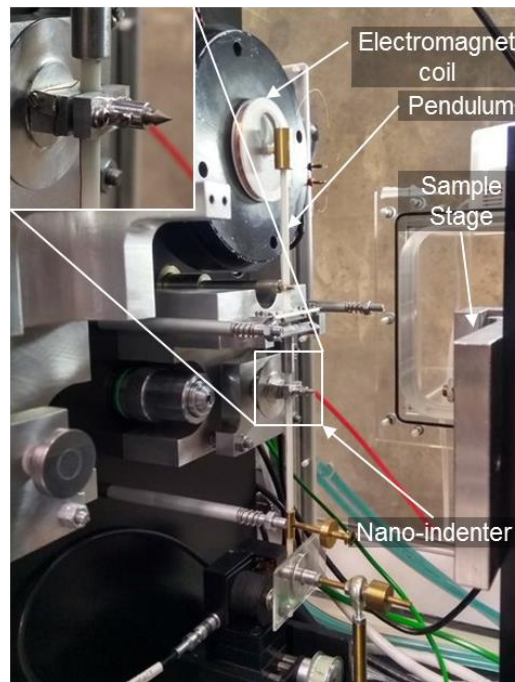


Figure 1.1 Micro-mechanical Raman spectroscopy setup

## 1.2 Nanoindentation setup

The stress-strain behavior for constitutive modeling was obtained using nanoindentation experiments. Figure 1.2 shows the nanoindentation setup used to obtain stress-strain curve. The indentation stress-strain curve was obtained through indentations performed using a spherical indenter of radius  $100\ \mu\text{m}$ . Such stress-strain curves provide a potential for understanding the material behavior which has been discussed by Field and Swain [13]. The procedure of obtaining indentation stress-strain is discussed later in the document.

A)



B)

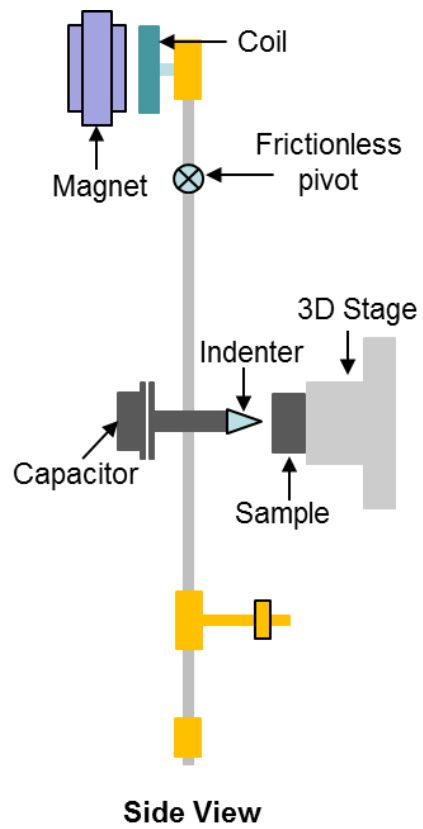


Figure 1.2 (A) Nanoindentation platform (Micro Materials Ltd., UK), (B) Schematic diagram of the nanoindentation platform

### 1.3 Machine learning model

Stresses induced inside ceramic particle due to matrix deformation are a function of several parameters such as particle geometry, particle orientation, distance from the free surface, and interface mechanics. Figure 1.3 shows the variation in geometry and orientation of such two particles inside epoxy resin matrix.

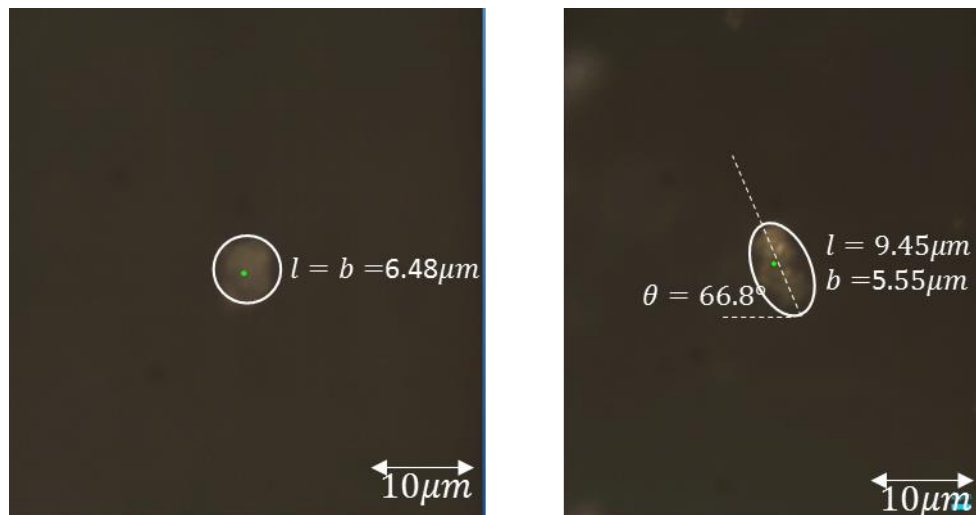


Figure 1.3 Different size and orientation of particles inside epoxy resin matrix

The study of stress concentration inside the particle with these many parameters poses an additional challenge of obtaining useful mathematical relationship for predicting stress during non-linear deformations. This problem was solved by training a machine learning model based on the results obtained from the FEM simulations. The data was structured with input as geometric parameters, average stress inside the particle, angle between principle stress direction and major axis of the particle, and the ratio of principal stresses (Figure 1.4 ) and output as stress magnitude in the matrix.

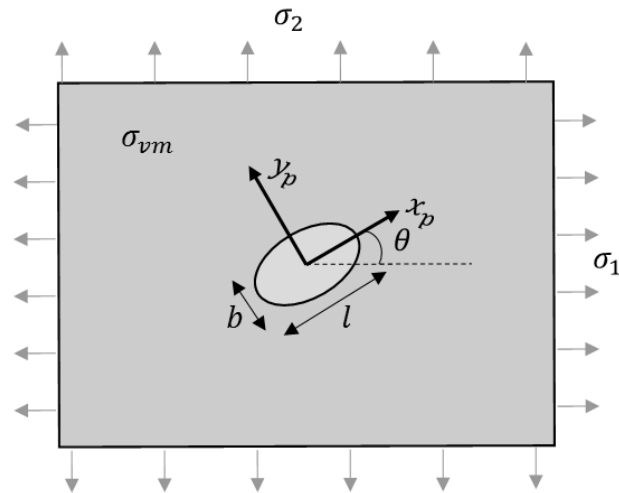


Figure 1.4 Schematic of elliptical particle inside stretched matrix

Due to non-linearity of the problem, the artificial neural network has been selected as the machine learning model. An artificial neural network [14-18] is a biologically inspired computational model formed from hundreds of single units, artificial neurons, connected with coefficients (weights) which constitute the neural structure. Although a single neuron can perform certain simple information processing functions, the power of neural computations comes from connecting neurons in a network (Figure 1.5).

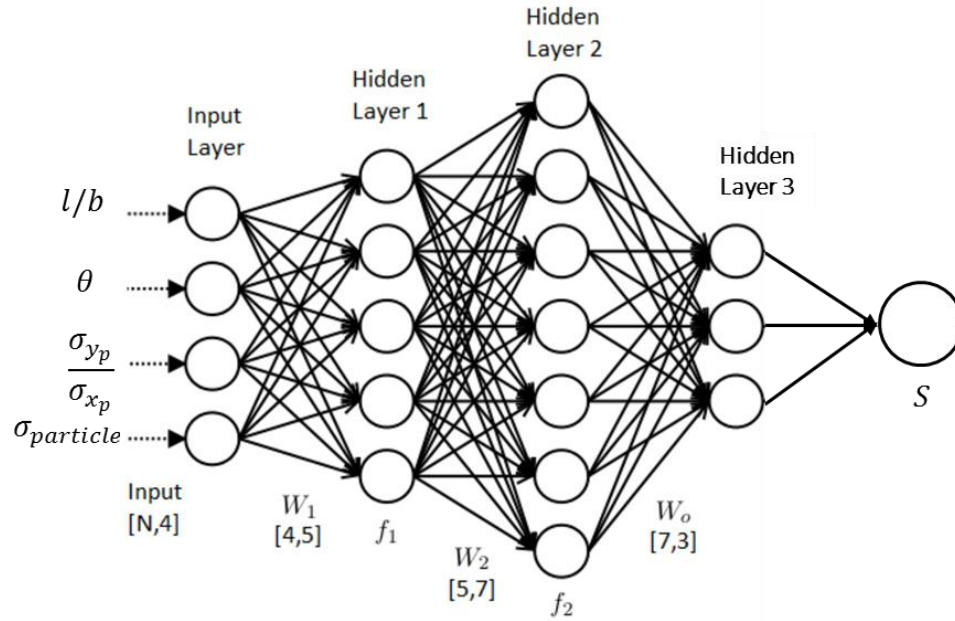


Figure 1.5 Schematic of artificial neural network

The artificial neuron is the building component of the artificial neural network designed to simulate the function of the biological neuron. The arriving signals, called inputs, multiplied by the connection weights (adjusted) are first summed (combined) and then passed through a transfer function to produce the output for that neuron. The activation function is the weighed sum of the neuron's inputs and the most commonly used transfer function are the sigmoid function and rectified linear units (ReLU) function [19]. Figure 1.6 shows the schematic for a signal neuron where  $a_k^{l-1}$  is an output from layer  $l-1$  and input  $k$  to the  $j^{th}$  element of layer  $l$ . In order to calculate the activation unit of this unit, the inputs are multiplied by the weights  $w_{jk}^l$  and biases  $b_j$  for that neuron. In matrix notation, unit value  $Z_j^l$  is

$$Z_j^l = \sum_k W_{jk}^l a_k^{l-1} + b_j^l. \quad (3)$$

The activation unit is the result of applying an activation function  $\sigma$  to obtain output  $a_l^l$  from the neuron and is defines as

$$a_j^l = \psi(Z_j^l). \quad (4)$$

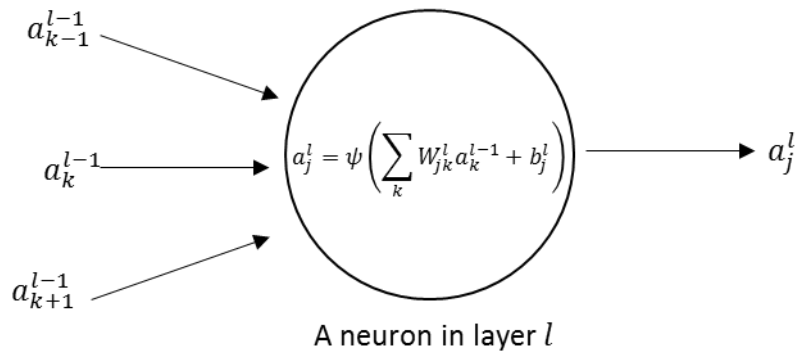


Figure 1.6 Schematic of a neuron

The activation function must be differentiable to be able to learn weights and biases using gradient descent. The ANN model for this work was implemented in Tensorflow [19] framework with ReLU as the activation function.

## CHAPTER 2. REVIEW OF LITERATURE

Micro-mechanical Raman spectroscopy is an excellent technique for non-destructive evaluation of stresses. Some of the important breakthroughs in the field of micro-mechanical Raman spectroscopy came through Ganesan et al [20], Anastassakis et al [21] and Wolf [22]. The relationship between stresses and Raman shift is governed by secular equations [20, 21] relating Raman shift and strain tensor which is further related to stresses using Hooke's law. Gan et al were able to separate stress induced Raman shift and temperature induced Raman shift for accurate calculation of thermal conductivity and mechanical stresses in silicon structures [23-26]. The stress were obtained using analytical relationships using elastic stress tensor and constitutive behavior of the material.

Since then, mechanical Raman spectroscopy has significantly evolved with direct stress measurements obtained without measuring strains using an imperial relationship between equivalent stress and change in Raman shift. This imperial relationship is linear for linear elastic deformations and correlation constant can be obtained through uniaxial tension/compression tests. The Raman shift increases for compressive uniaxial or biaxial stress and decreases for tensile stress. Such relationship has been used to measure change in thermal conductivity of bovine cortical bone due to induced stresses [12] and stress distribution due to bending of a notch tip at room temperature [5, 6, 27] as well as elevated temperature [7, 8] to model plastic behavior of the material. Direct stress measurements using nanomechanical Raman spectroscopy has been extensively used to determine interface mechanics [4, 10, 28-30] and to model high strain rate failures and temperature rise for explosives and polymer composite [1, 2].

The imperial relationship between change in Raman shift and equivalent stress is not generally linear for non-linear behavior [31] which restricts the experimental measurement of stress during plastic deformation. A piece-wise imperial correlation between stresses and Raman shift can be obtained but difficulties in calibrating stress during plastic deformation limits the experimental study of large deformations. Up to author's knowledge, this is a first attempt to resolve stress in nonlinear domain by dispersion of particles inside the epoxy resin matrix where stress state of particles is used to collect information of stress induced inside epoxy resin matrix. In this work strontium titanate ceramic particles dispersed inside epoxy resin matrix were used to obtain stress information using micro-mechanical Raman spectroscopy. Since, the ceramic particles have higher elastic modulus compared to that of epoxy matrix, the stress induced inside particle due to stretching of matrix, remains in elastic domain.

This technique can be used for measurement stresses in materials with large plastic deformations either by dispersion of particles inside the matrix or by deposition of thin layer of ceramic/epoxy composite on the surface. By, deposition of composite material on the surface, the stress in the composite layer can be correlated to stress in substrate by equating strains on the interface [5-8].

## CHAPTER 3. RESEARCH METHODOLOGY

### 3.1 Sample preparation

The composite samples were fabricated by dispersion of 1% v/v of strontium titanate particles from Sigma Aldrich inside epoxy resin system by rotating in the planetary centrifuge for 10 mins. The mixture was kept inside the vacuum chamber for 30 mins to remove any trapped air pockets. The mixture was further cured under vacuum oven for 5 hrs. Figure 3.1 shows the bending test sample analyzed in this work for stress distribution measurements and the sample dimensions. The dimensions were verified by an elastic finite element analyses to make sure that the contact mechanics at boundary conditions don't affect the stress distribution at the notch. The stress distribution by finite element analysis when 10N force is applied over the length of 0.5mm above the notch is shown in Figure 3.2.

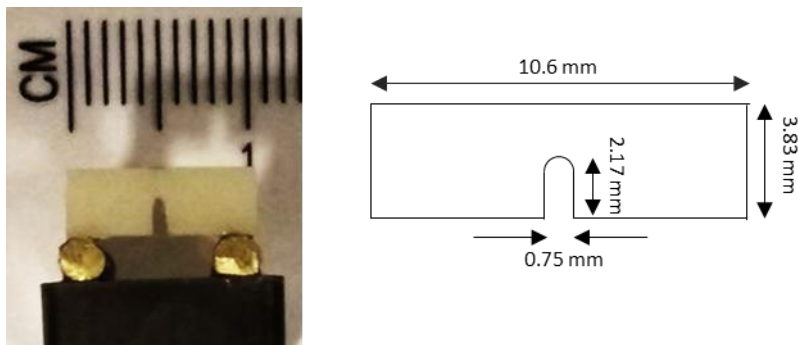


Figure 3.1 Bending test sample

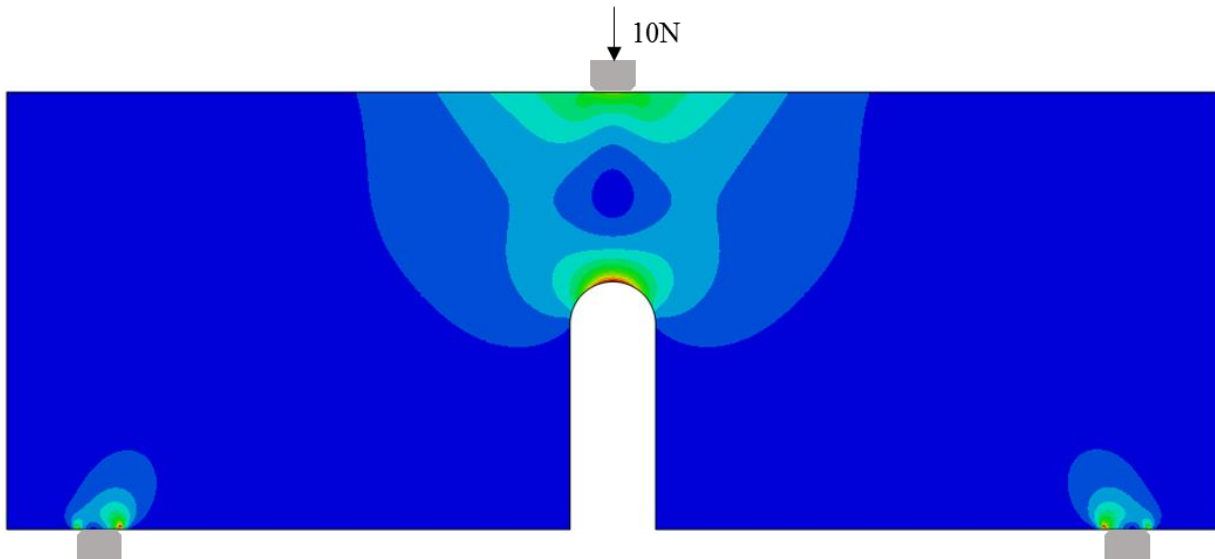


Figure 3.2 Stress distribution using finite element method

### 3.2 Raman Spectroscopy

The inclusion of strontium titanate particles inside the epoxy resin matrix was verified through Raman spectroscopy. Figure 3.3 shows the Raman spectrum for strontium titanate particles, epoxy resin and strontium titanate epoxy composite. For epoxy resin system, the peak of C-H bond stretching at  $639.48\text{ cm}^{-1}$  was used for micro-mechanical Raman calibration while for strontium titanate peak at  $247.95\text{ cm}^{-1}$  was used for micro-mechanical Raman spectroscopy.

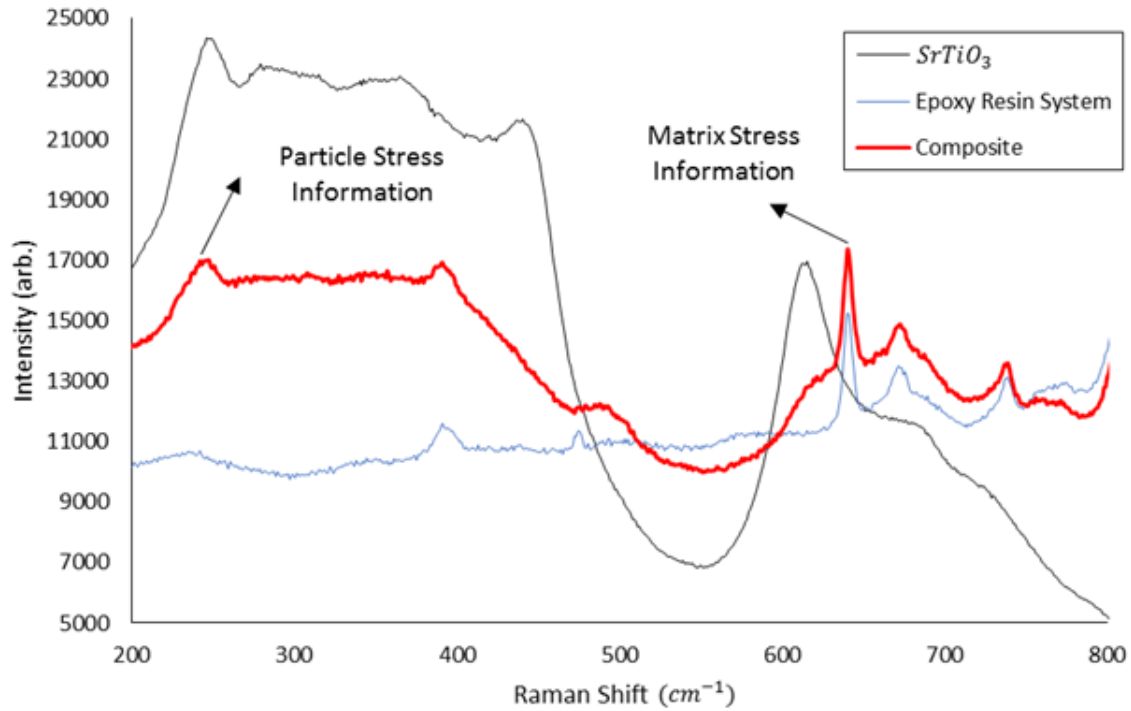


Figure 3.3 Raman spectrum for strontium titanate particles, epoxy resin system and composite

### 3.3 Micro-mechanical Raman spectroscopy

The micro-mechanical Raman spectroscopy is a technique to measure stress at meso and micro scales. The shift in Raman peak is a function of applied stress where Raman shift between stressed and unstressed state is defined as

$$w_{no\ stress} = \left( \frac{1}{\lambda_i} - \frac{1}{\lambda_{no\ stress}} \right), \quad (5)$$

$$w_{stress} = \left( \frac{1}{\lambda_i} - \frac{1}{\lambda_{stress}} \right) \quad (6)$$

where,  $\lambda_i$  is the wavelength of incident light and  $\lambda_{no\ stress}$  and  $\lambda_{stress}$  are the wavelength of scattered light at unstressed and stress state respectively. The change in Raman shift given by

equation (7) is linearly proportional to equivalent stress. This relationship is given in equation (8) [3, 4, 24, 32] where C is material constant obtained through experiments.

$$\Delta w = w_{stress} - w_{no\ stress} \quad (7)$$

$$\sigma = C \Delta w \quad (8)$$

The accurate calculation of the change in Raman shift is very important to obtain correct stress values based on equation (8). This is achieved by using Lorentz fitting on Raman spectrum of interested Raman shift. Figure 3.4 Shows the Lorentz fitting on Raman spectrum for C-H bonds stretching in the epoxy resin at  $640.39 \pm 0.06 \text{ cm}^{-1}$ .

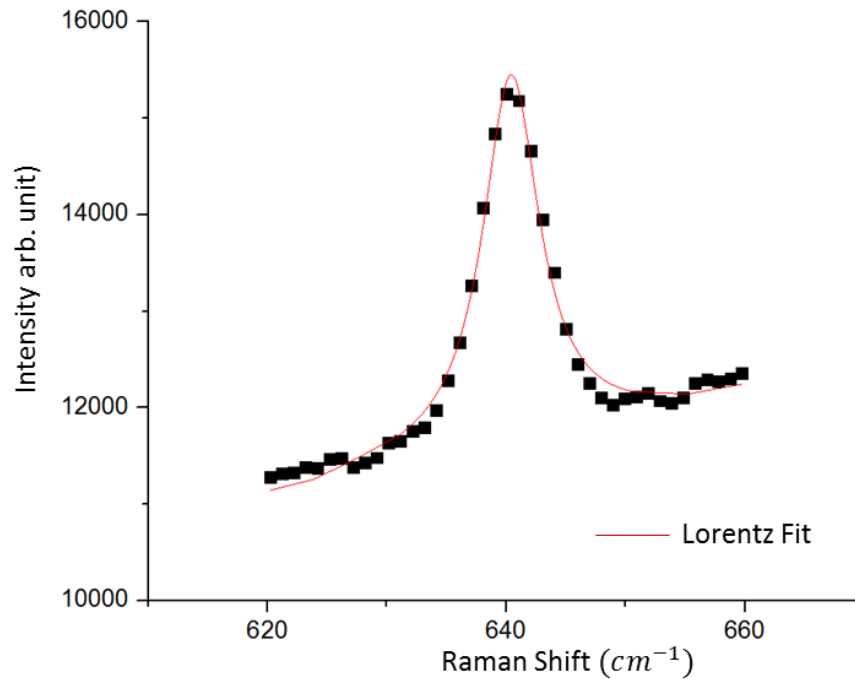


Figure 3.4 Raman spectrum for C-H bond stretching in epoxy resin

For epoxy resin system, the peak of C-H bond stretching was used for micro-mechanical Raman spectroscopy where the material constant for epoxy resin ( $C_{Epoxy}$ ) was obtained by uniaxial compression experiments.

For strontium titanate peak at  $247.95\text{ cm}^{-1}$  was used for micro-mechanical Raman spectroscopy where material constant was obtained using 3-point bending test. The composite sample with a circular notch of diameter 0.75 mm and thickness 0.8 mm was analyzed under 3-point bending. The sample was placed on two rigid rollers with a distance of 8 mm as shown in Figure 3.5. The sample was fixed on the rollers, while a distributed load was applied over 0.5 mm length above the notch using a punch.

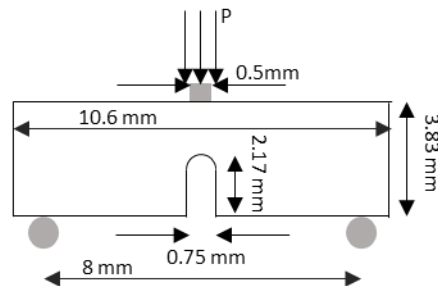


Figure 3.5 Bending Test Sample

#### 3.4 Material characterization

Mechanical properties of the epoxy resin matrix and the composite material were determined based on nanoindentation stress-strain curve. The use of indentation stress-strain curve has been shown to be appropriate by Field and Swain [13] for understanding the material behavior at the microscale. The indentations were performed using a spherical-indenter of radius  $100\ \mu\text{m}$  with loads ranging from 50 mN – 400 mN. Indentations were performed on a nanoindentation setup from Micro Materials Ltd., UK. The indentation stress strain curve was obtained from the loading part of the load displacement curve of indentations using the approach of [33, 34]. The indentation stress and indentation strain relation are defined as

$$\sigma_{indent} = \frac{P}{\pi a_c^2}, \text{ and} \quad (9)$$

$$\varepsilon_{indent} \approx \frac{h_e}{2.4a_c}. \quad (10)$$

By Hertz theory [35], the elastic penetration depth  $h_e$  is calculated as

$$h_e = \left( \frac{3P}{4E_{eff}} \right)^{\frac{2}{3}} \left( \frac{1}{R_i} \right)^{\frac{1}{3}}. \quad (11)$$

Here,  $E_{eff}$  is the reduced modulus and  $R_i$  is the radius of the indenter ( $100 \mu\text{m}$ ).  $E_{eff}$  is expressed as:

$$\frac{1}{E_{eff}} = \frac{1-v_s^2}{E_s} + \frac{1-v_i^2}{E_i}. \quad (12)$$

Here,  $E_s$  and  $v_s$  are Young's modulus and Poisson's ratio for the sample while  $E_i$  and  $v_i$  are Young's modulus and Poisson's ratio for indenter. The contact depth  $h_c$  is given as

$$h_c = h_t - 0.5 \times \left( \frac{3P}{4E_{eff}} \right)^{\frac{2}{3}} \left( \frac{1}{R} \right)^{\frac{1}{3}}. \quad (13)$$

Here,  $h_t$  is the total indentation depth obtained from experiment and  $P$  is the load observed at depth  $h_t$ . Based on  $h_t$ , the contact radius  $a_c$  is calculated as

$$a_c = \sqrt{2h_t R - h_t^2}. \quad (14)$$

For the nanoindentation experiment, the initial point of contact can be affected by artifacts like surface roughness, the oxide layer, etc. These artifacts can lead to significant error in calculation of stress during initial part of elastic deformation. This error was corrected by determination the effective point of contact [33].

## CHAPTER 4. RESULTS

### 4.1 Material characterization

The mechanical properties of the epoxy resin matrix and epoxy-ceramic composite material were determined using indentation stress-strain curve. The indentation stress-strain curve was obtained using the loading part of the indentation load vs depth curve. The indentations were performed using a spherical-indenter of radius 100  $\mu\text{m}$  with loads ranging from 50 mN - 400 mN. The load-depth curve for epoxy resin and composite sample for the maximum load of 400 mN is shown in Figure 4.1 .

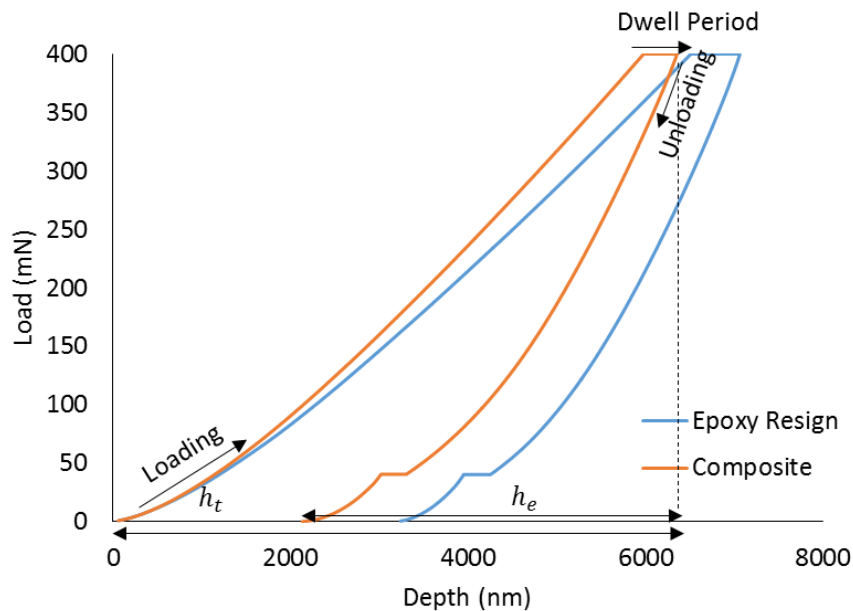


Figure 4.1 Indentation load vs depth for epoxy resin and strontium titanate epoxy composite.

It can be observed from Figure 4.1 that the inclusion of ceramic particles to the epoxy resin increase the resistance of the material to the deformation. At the same maximum load of 400 mN, the epoxy resin shows higher indentation depth compared to the composite material.

By Hertz theory [35], the elastic penetration depth  $h_e$  is calculated by equation (15) as

$$h_e = \left( \frac{3P}{4E_{\text{eff}}} \right)^{\frac{2}{3}} \left( \frac{1}{R_i} \right)^{\frac{1}{3}}. \quad (15)$$

Here,  $E_{\text{eff}}$  is the reduced modulus and  $R_i$  is the radius of the indenter (100  $\mu\text{m}$ ).  $E_{\text{eff}}$  is expressed as:

$$\frac{1}{E_{\text{eff}}} = \frac{1-v_s^2}{E_s} + \frac{1-v_i^2}{E_i}. \quad (16)$$

Here,  $E_s$  and  $v_s$  are Young's modulus and Poisson's ratio for the sample while  $E_i$  and  $v_i$  are Young's modulus and Poisson's ratio for indenter. The contact depth  $h_c$  is given as:

$$h_c = h_t - 0.5 \times \left( \frac{3P}{4E_{\text{eff}}} \right)^{\frac{2}{3}} \left( \frac{1}{R} \right)^{\frac{1}{3}}. \quad (17)$$

Here,  $h_t$  is the total indentation depth obtained from experiment and  $P$  is the load observed at the depth  $h_t$ . Based on  $h_t$ , the contact radius  $a_c$  is calculated as

$$a_c = \sqrt{2h_t R - h_t^2}. \quad (18)$$

The indentation stress and indentation strain are defined as

$$\sigma_{\text{indent}} = \frac{P}{\pi a_c^2}, \text{ and} \quad (19)$$

$$\varepsilon_{\text{indent}} \approx \frac{h_t}{2.4a_c}. \quad (20)$$

After obtaining stress-strain curve using load vs depth curve, the zero point correction was performed based on the research work of Kalidindi et al [33, 34] to obtain correct indentation stress-strain curve as shown in Figure 4.2 .

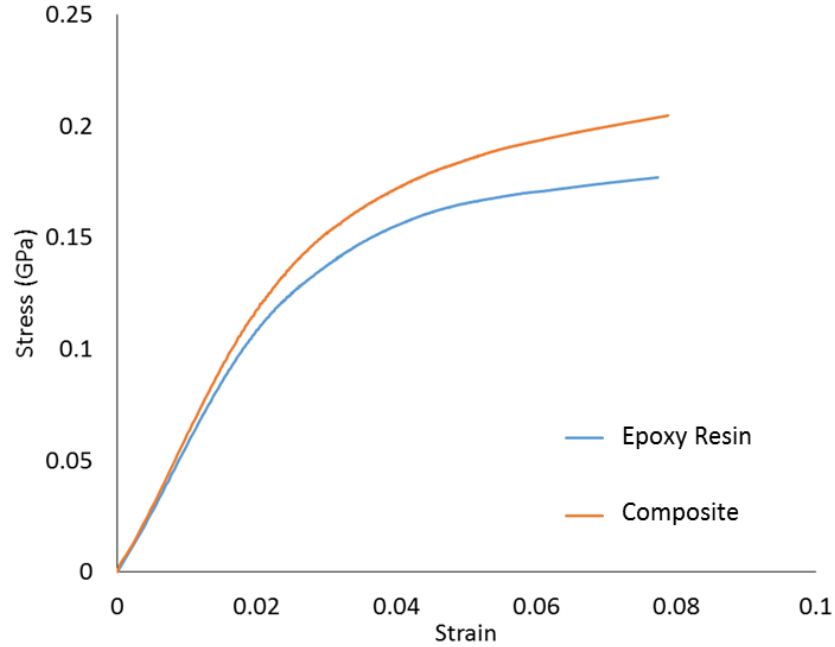


Figure 4.2 Indentation stress-strain curve for epoxy resin and strontium titanate epoxy composite

The constitutive model in the non-linear elastic region is defined by

$$\sigma = \begin{cases} E \varepsilon_{VM} & \varepsilon_{VM} < \varepsilon_{PEL} \\ A_1 \varepsilon_{VM}^{n_1} & \varepsilon_{PEL} \leq \varepsilon_{VM} < \varepsilon_{inter} \\ A_2 \varepsilon_{VM}^{n_2} & \varepsilon_{inter} \leq \varepsilon_{VM} < \varepsilon_Y \end{cases} \quad (21)$$

where  $\varepsilon_{PEL}$  is strain a proportionality elastic limit,  $\varepsilon_{inter}$  is intermediate strain in non-linear elastic region,  $\varepsilon_Y$  is strain at yield point and  $\varepsilon_{VM}$  is equivalent Von-Misses strain given by

$$\varepsilon_{VM} = \frac{2}{3} \sqrt{\frac{3}{2}(e_{xx}^2 + e_{yy}^2) + \frac{3}{4}\gamma_{xy}^2} \quad (22)$$

$$e_{xx} = \frac{2}{3}\varepsilon_{xx} - \frac{1}{3}\varepsilon_{yy}$$

$$e_{yy} = -\frac{1}{3}\varepsilon_{xx} + \frac{2}{3}\varepsilon_{yy}$$

$$\gamma_{xy} = 2\varepsilon_{xy}$$

Based on the indentation stress-strain curve, the constants in equation (21) for epoxy resin and composite obtained are:

Table 4.1 Constitutive model parameters for epoxy resin matrix

<b>Constants</b>	<b>Values</b>
E (Elastic Modulus)	$5.787 \pm 0.117$ GPa
$\varepsilon_{PEL}$	0.016
$\varepsilon_Y$	0.04
$\varepsilon_{inter}$	0.025
$A_1$	1.955 GPa
$n_1$	0.745
$A_2$	0.71 GPa
$n_2$	0.47

Table 4.2 Constitutive model parameters for composite

<b>Constants</b>	<b>Values</b>
E (Elastic Modulus)	$6.244 \pm 0.033$ GPa
$\varepsilon_{PEL}$	0.016
$\varepsilon_Y$	0.04
$\varepsilon_{inter}$	0.025
$A_1$	2.483 GPa
$n_1$	0.786
$A_2$	0.819 GPa
$n_2$	0.484

#### 4.2 Micro-mechanical Raman spectroscopy

For epoxy resin system, the calibration for change in Raman shift of  $640.39 \text{ cm}^{-1}$  was obtained using uniaxial compression experiment of a sample with area  $3.07 \times 3.48 \text{ mm}^2$  and length 5 mm. Figure 4.3 shows that change in Raman shift with compressive stress for epoxy resin where material constant ( $C_{Epoxy}$ ) of  $222.22 \text{ MPa} - \text{cm}$  was obtained. This change in Raman shift was used to obtain stress distribution around the notch sample using 3-point bending test using micro-mechanical Raman spectroscopy. A constant load of 10 N was applied above the notch using punch and in-situ Raman spectroscopy was performed over the notch area. The stresses were obtained as,

$$\sigma = C_{Epoxy} \times \Delta\omega. \quad (23)$$

Figure 4.4 shows the stress distribution around the notch for the composite sample for 10 N applied load.

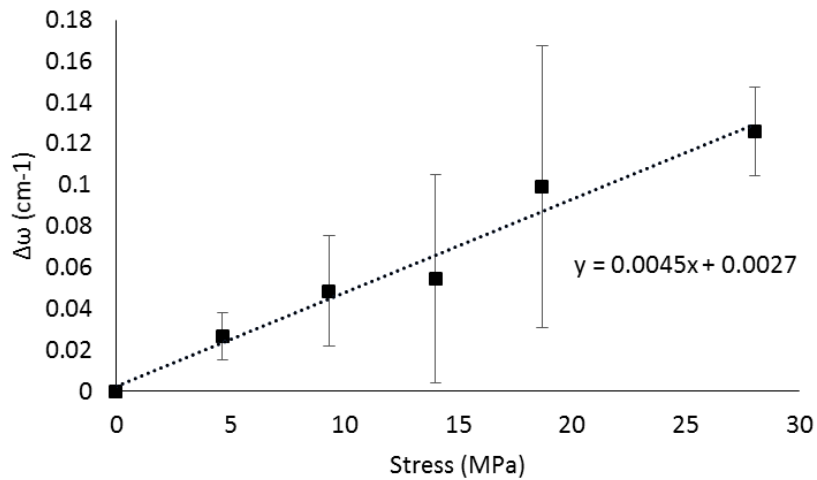


Figure 4.3 Change in Raman shift for epoxy resin with compressive stress.

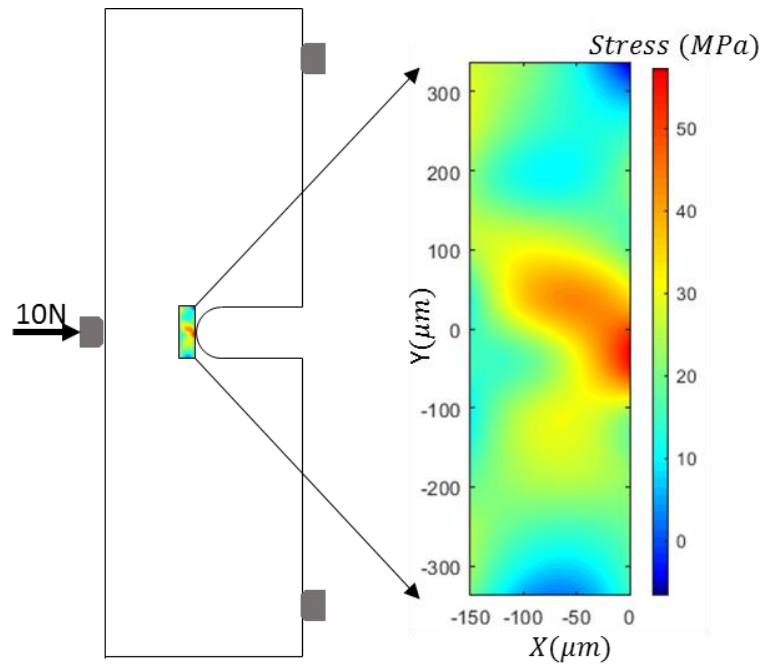


Figure 4.4 Stress (tensile) distribution around notch using micro-mechanical Raman spectroscopy.

The maximum equivalent tensile of 58 N was observed for 10 N applied load. As this stress is below the stress at proportionality elastic limit, the stresses inside the sample can be assumed in linear elastic domain. It is important for stresses to be in the linear elastic domain for calibration of Raman shift for strontium titanate particles as it is shown later in the results that stress concentration factor of 1.45 can be assumed for spherical particles to correlate between average stress inside the particle and nominal stress inside matrix around it.

The change in Raman shift for strontium titanate particle can be calibrated with stress-induced inside particle due to stretching of epoxy resin matrix around it. With stress concentration factor of 1.45 in the linear elastic domain for spherical particle, the material constant ( $C_{SrTiO_3}$ ) can be obtained as:

$$C_{SrTiO_3} = 1.45 \times C_{Epoxy} \times \frac{\Delta\omega_{Epoxy}}{\Delta\omega_{SrTiO_3}} \quad (24)$$

Using equation (24), the obtained  $C_{SrTiO_3}$  value was  $85.68 \text{ MPa} - \text{cm}$  and the stress distribution around strontium titanate particle of diameter  $6.48 \mu\text{m}$  is shown in Figure 4.5 .

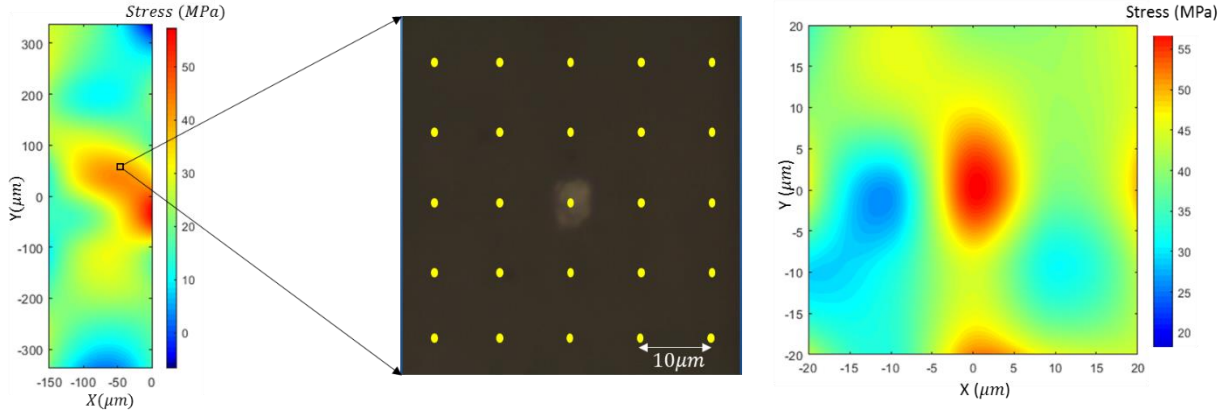


Figure 4.5 Stress (Tensile) distribution around strontium titanate particle

### 4.3 Finite element method

The finite element method for the epoxy resin and composite material was implemented in ABAQUS using a custom material subroutine. Since the deformation of the epoxy system is recoverable till yield stress and small stains of 4% at yield point were observed from indentation stress-strain curve, a pointwise linear elastic model was used for FEM analysis. This model is similar to the multi-linear elastic model, but the linear relationship after the proportional elastic limit was replaced by the power law relation as shown given in Equation (21). Hence, the tangential elastic modulus for the composite and epoxy resin can be defined as:

$$E_t = \begin{cases} E & \varepsilon_{VM} < \varepsilon_{PEL} \\ A_1 n_1 \varepsilon_{VM}^{n_1-1} & \varepsilon_{PEL} \leq \varepsilon_{VM} < \varepsilon_{inter} \\ A_2 n_2 \varepsilon_{VM}^{n_2-1} & \varepsilon_{inter} \leq \varepsilon_{VM} < \varepsilon_Y \end{cases} \quad (25)$$

The tangential stiffness matrix for the plain stress problem was defined in UMAT subroutine as:

$$S_{ij} = \frac{E_t}{(1-\nu^2)} \begin{bmatrix} 1 & \nu & 0 \\ \nu & 1 & 0 \\ 0 & 0 & \frac{1-\nu}{2} \end{bmatrix}. \quad (26)$$

ABAQUS has many suitable elements type for finite element analysis such as truss element, beam element, shell element, etc. Since the main purpose of this model is to simulate plain stress problems, the quadrilateral and triangular shell elements were used. The implemented model was tested on a uniaxial tension problem. Figure 4.6 (A) shows the mesh using quadrilateral shell element for beam under the uniaxial tensile stress. It can be seen in Figure 4.6 (B), that the results from the finite element method closely follow the experimental curve.

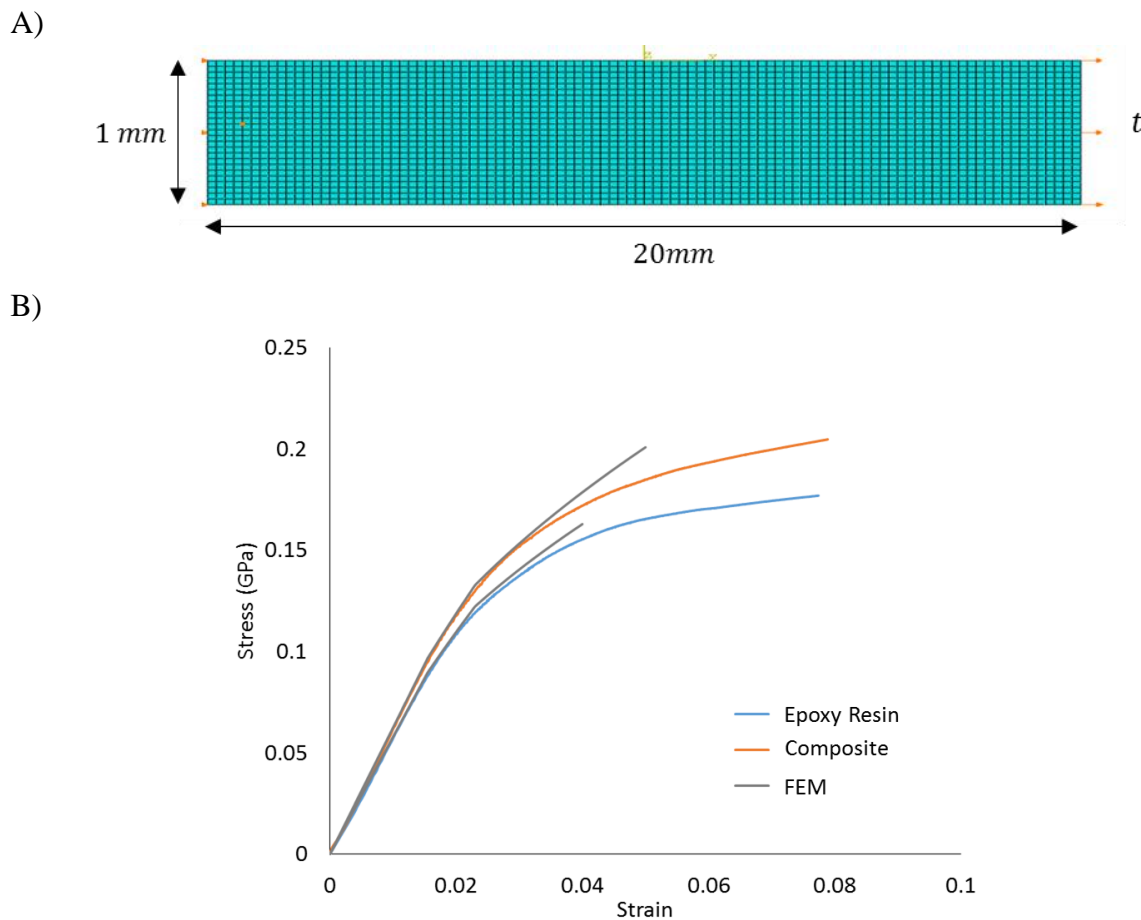


Figure 4.6 A) Mesh for beam under uniaxial tension B) Comparison of results from the FEM model and experiments

The FEM model defined above was used to quantify the variation in stress concentration factor due to the different orientation of the particle with principal stress directions, the geometry of the particle, nominal stress inside the matrix and the ratio of principal stresses. The Stress concentration factor for this study is defined as

$$S_{factor} = \frac{\text{Average VM stress inside particle}}{\text{Nominal stress inside matrix}} \quad (27)$$

Figure 4.7 shows the mesh generated for an elliptical particle of the length of major and minor axis as 4mm and 2mm respectively. The major axis of the particle is oriented at  $45^\circ$  to X-axis. The mesh is generated with quadrilateral shell elements away from the particle and refined meshed with triangular shell elements inside and around the particle. The length of the matrix was kept sufficient enough so that the stress concentration inside matrix due to the particle is not observed at the boundaries.

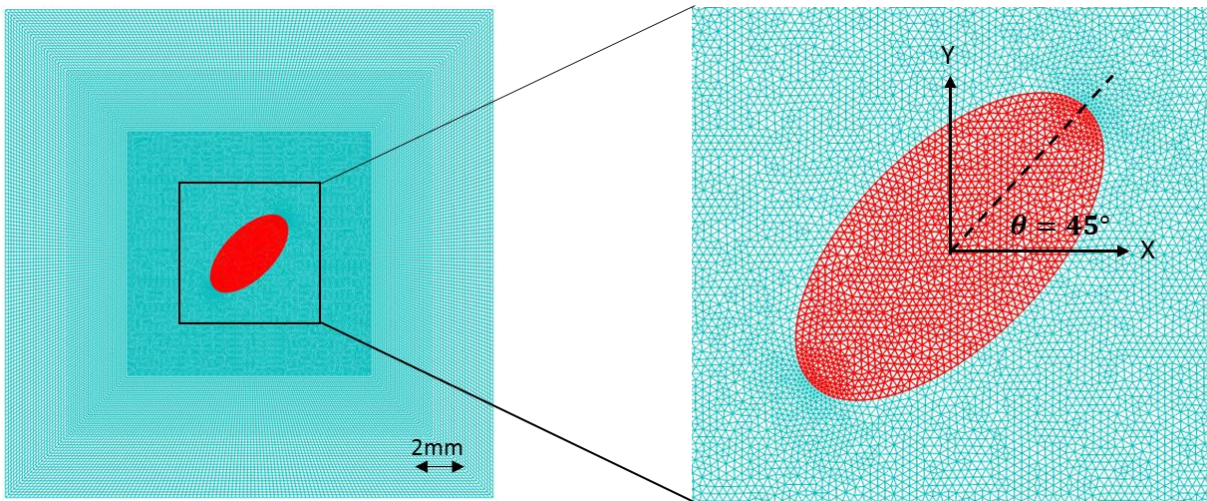


Figure 4.7 Mesh for particle inside epoxy resin matrix

The convergence of the model was checked by computing the strain energy with increasing number of elements for tensile stress of 100 MPa along X-axis. Figure 4.8 (A) shows schematic of an elliptical particle inside epoxy resin matrix and Figure 4.8 (B) shows the convergence of strain

energy with increasing number of elements where the change in strain energy is not significant above 50 thousand elements. Therefore, more than 60 thousand elements were used for this study.

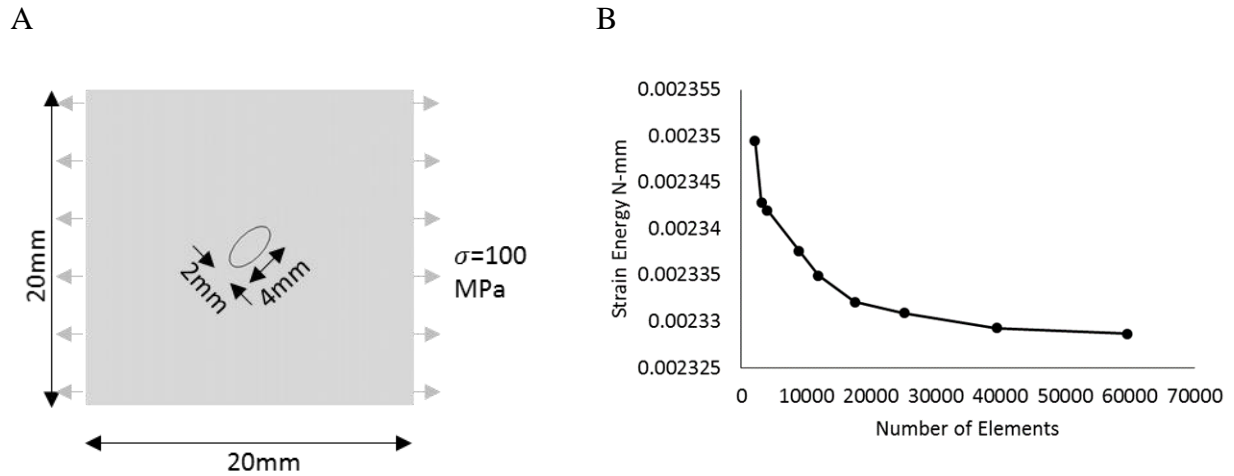


Figure 4.8 A) Schematic of elliptical particle inside epoxy resin matrix B) Convergence of model with the number of elements

Figure 4.9 shows Stress distribution around elliptical particle using FEM for schematic shown in Figure 4.8 .

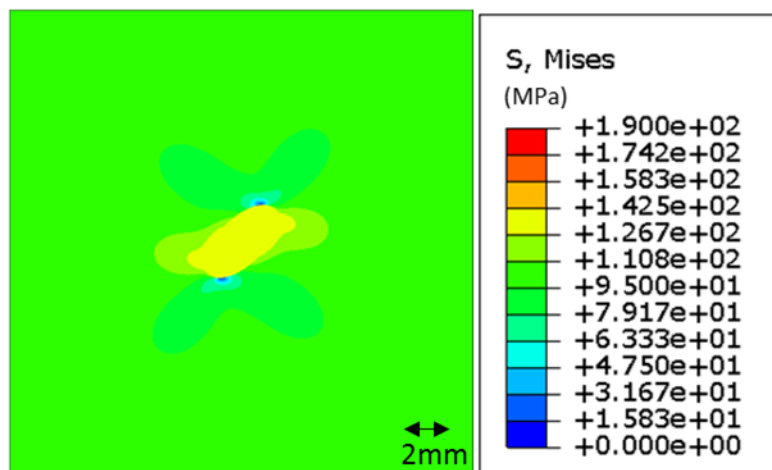


Figure 4.9 Stress distribution around elliptical particle from FEM

Figure 4.10 shows the comparison of results from the finite element method with the stress distribution obtained using micro-mechanical Raman spectroscopy. The defined finite element method was validated using the results from micro-mechanical Raman spectroscopy as the stress distribution from the finite element method is close to experimental stress distribution.

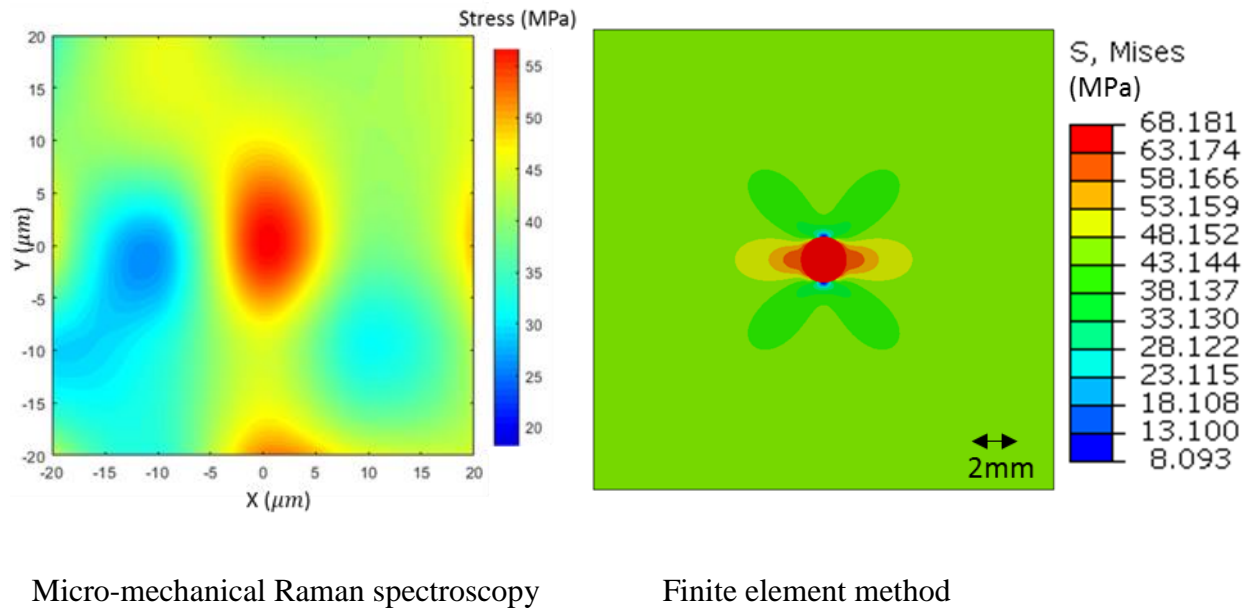


Figure 4.10 Validation of FEM results with experimental results

Since the FEM model was verified, it was used to study the effect of the orientation of the particle with principal stress directions, the geometry of the particle, nominal stress inside the matrix and the ratio of principal stresses. Figure 4.11 shows schematic of particle inside epoxy resin matrix. The variation due to these variables was studied using parametric simulation in ABAQUS where variables and their range are defined in Table 4.3.

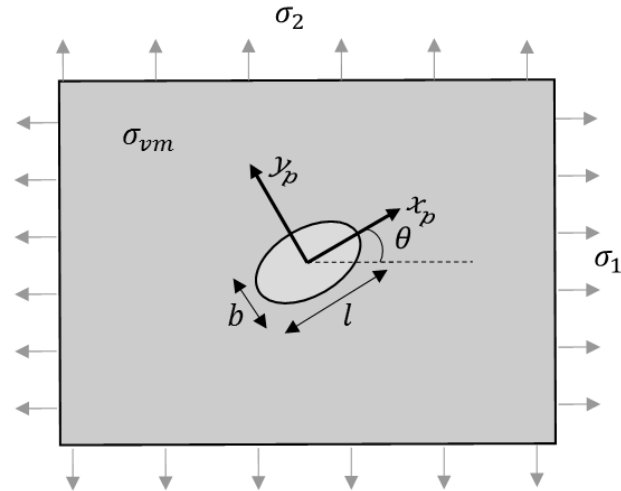


Figure 4.11 Schematic of particle inside epoxy resin matrix

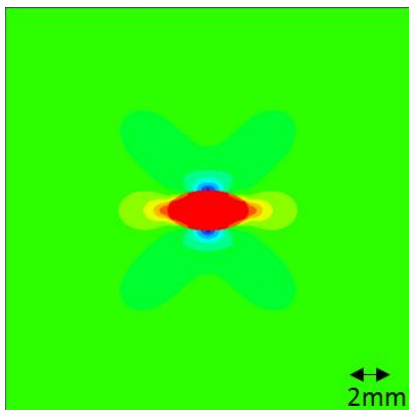
Table 4.3 Variable used for parametric simulation

	<b>Variable</b>	<b>Range</b>
1.	$\sigma_{vm} = \sqrt{\frac{\sigma_1^2 + \sigma_2^2 + (\sigma_1 - \sigma_2)^2}{2}}$	$-100 \leq \sigma \leq 100 \text{ MPa}$
2.	$r = \frac{\sigma_1}{\sigma_2}$	$-1 \leq r \leq 1$
3.	$\theta = \text{angle of major axis with X-axis}$	$0^\circ \leq \theta \leq 90^\circ$
4.	$\frac{l}{b} = \frac{\text{Length of Major Axis}}{\text{Length of Minor Axis}}$	$1 \leq \frac{l}{b} \leq 2$

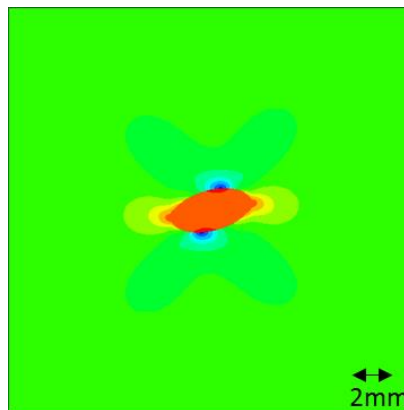
Figure 4.12 shows the variation of stress concentration inside elliptical particle with the orientation of major axis with principle stress direction in matrix for  $\sigma_{vm} = 100 \text{ MPa}$ ,  $r = 0$  and

$l/b = 2$ . The stress concentration factor for this configuration varies from 1.897 to 1.265 with change in orientation angle from  $0^\circ$  to  $90^\circ$ .

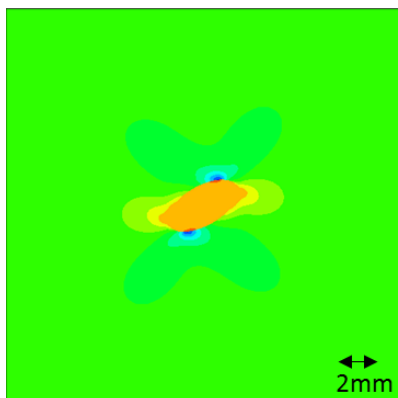
A)  $\theta = 0^\circ$



B)  $\theta = 15^\circ$



C)  $\theta = 30^\circ$



D)  $\theta = 45^\circ$

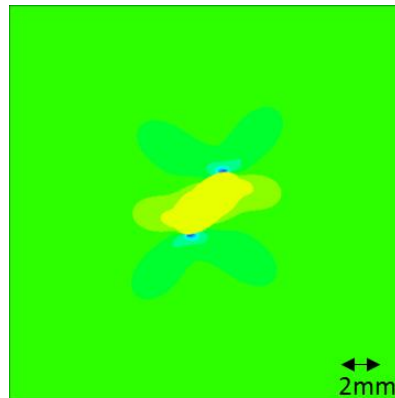
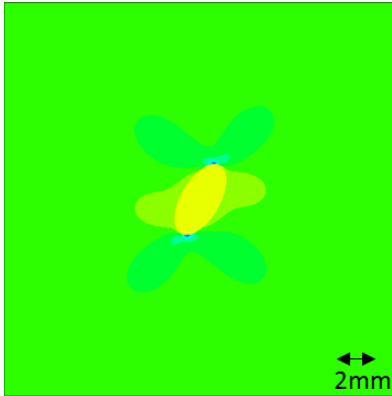
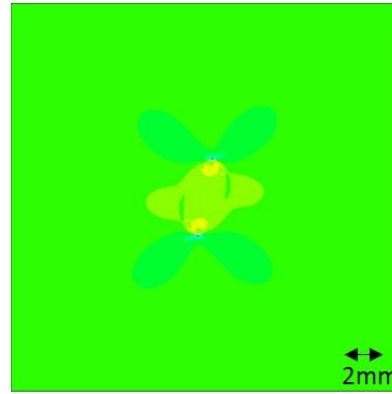
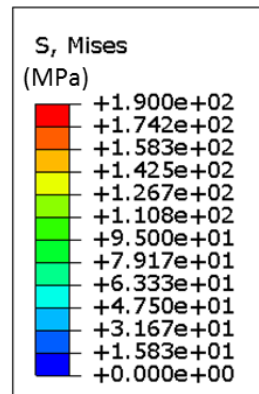
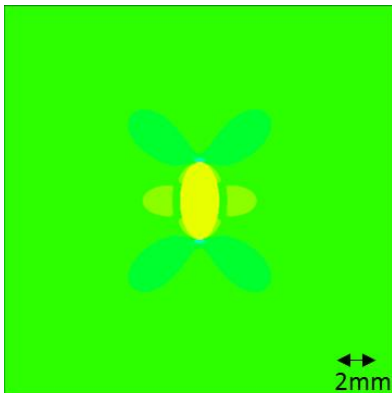


Figure 4.12 Variation of stress concentration with the orientation of major axis of the particle with principle stress direction.

Figure 4.12 continued

E)  $\theta = 60^\circ$ F)  $\theta = 75^\circ$ G)  $\theta = 90^\circ$ 

Similarly, the variation of stress concentration factor with  $r$ ,  $\sigma_{vm}$  and  $l/b$  are shown in Figure 4.13. Figure 4.13 (A) shows the variation of stress concentration factor with orientation angle for a case when the tensile stress of magnitude 68.64 MPa is applied in X-direction and tensile stress of magnitude 13.73 MPa is applied in Y-direction. The maximum stress concentration factor of 1.91 and minimum of 1.21 was observed for  $l/b$  ratio of 2. It should be notes that the maximum Von-Misses stress in the epoxy resin matrix is below stress at PEL. Figure 4.13 (B) shows the variation

of stress concentration factor with the magnitude of nominal stress in epoxy resin matrix at different values of  $r$ , the orientation angle of  $45^\circ$  and  $l/b$  ratio of 2. It can be seen that stress concentration factor remains constant during linear elastic deformation but decreases after stress at PEL. Figure 4.13 (C) shows the variation of stress concentration factor with orientation angle for a case when tensile stress of magnitude 98 MPa is applied in X-direction and stress tensile stress of magnitude 19.6 MPa is applied in Y-direction. The maximum stress concentration factor is slightly lower that observed in Figure 4.13 (A) as nominal stress in epoxy matrix is above stress at PEL. Figure 4.13 (D) shows that for a spherical particle inside the matrix, the change in stress concentration factor varies between 1.425 to 1.448 for decreasing values of  $r$ . This variation in stress concentration factor is very less compared to studies discuss above. Therefore, a constant value of 1.45 for stress concentration factor was used for calibration of Raman shift for spherical strontium titanate particle in elastic deformation.

A

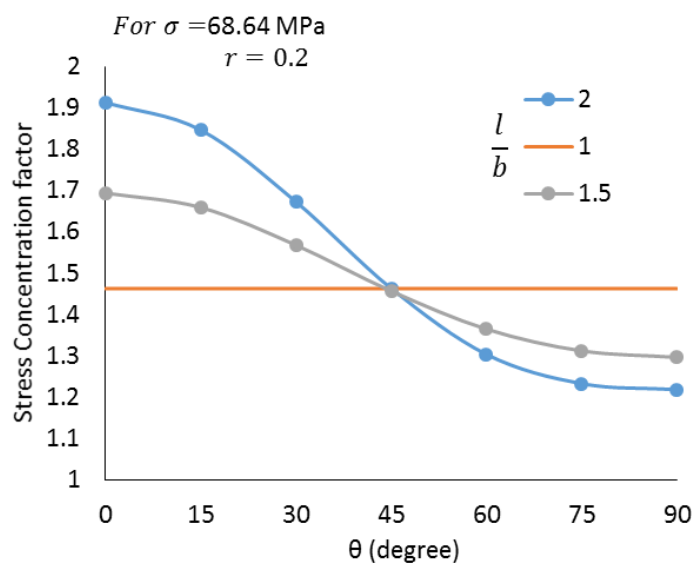
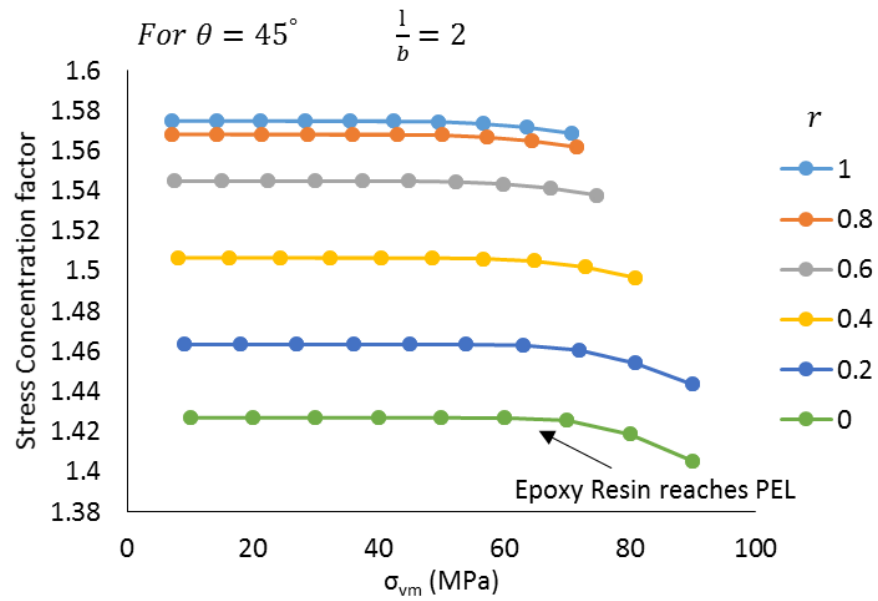


Figure 4.13 Variation of stress concentration factor with A)  $\theta$  B)  $\sigma_{vm}$  and  $r$  C)  $l/b$   
D)  $\sigma_{vm}$  and  $r$  for  $l/b = 1$

Figure 4.13 continued

B



C

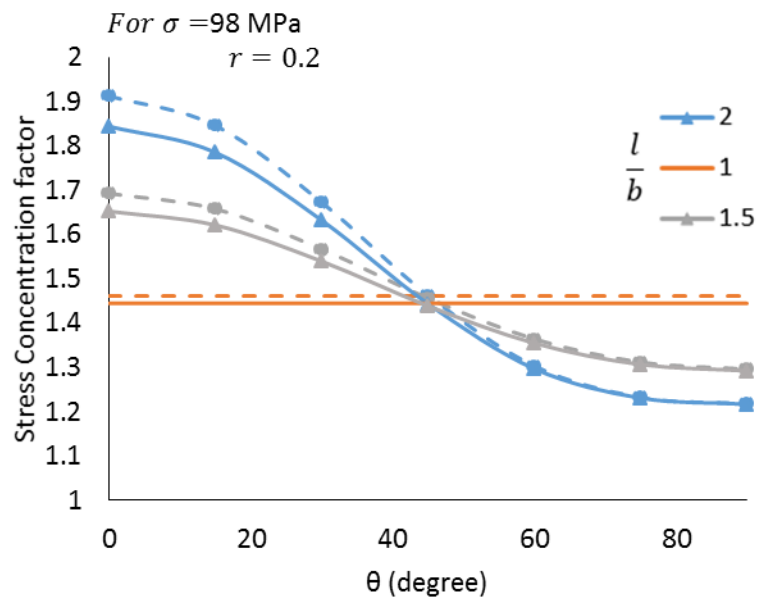
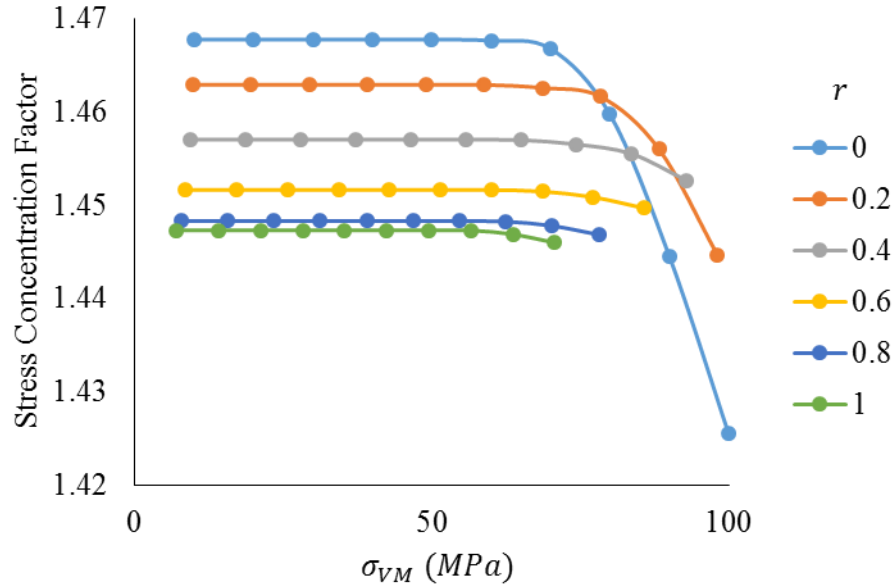


Figure 4.13 continued

D



#### 4.4 Machine learning algorithm

The data obtained from finite element methods shows the variation of stress concentration inside the particle due to various factors. For predicting stress inside matrix from average stress inside particle required a model which can invert the behavior observed in finite element data. The variation of stress concentration factor with the orientation of the particle with principal stress directions, the geometry of the particle, nominal stress inside the matrix and the ratio of principal stresses can be modeled into a machine learning algorithm using neural networks as:

$$a_j^l = \psi(Z_j^l) \quad (28)$$

where,

$$Z_j^l = \sum_k w_{jk}^l a_k^{l-1} + b_j^l.$$

The training set of machine learning model was based on results from finite element method. The input to the neural network is  $\sigma_{vm}$ ,  $r$ ,  $\theta$ ,  $l/b$  and model was optimized to predict the stress concentration factor. The neural network model was implemented in the TensorFlow framework with 3 hidden layers and 20 neuron each layer with mean square error as the objective function. The model was optimized with combination of cross-validation and random shuffling of data after one complete cross-validation. Figure 4.14 shows decrease in the log-mean square error with training cycles. The data was re-shuffled and trained for 200 times to achieve least mean square.

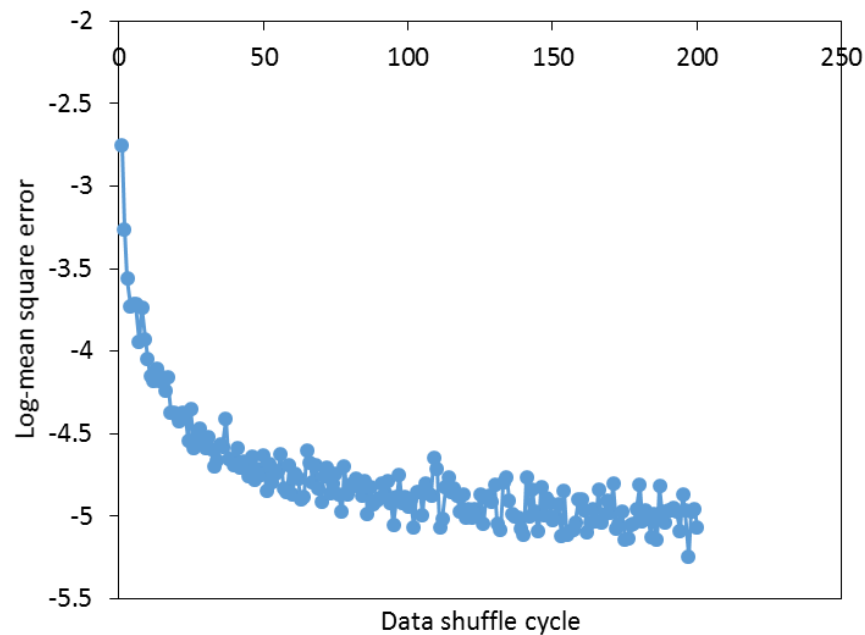


Figure 4.14 Log mean square error with training

After model optimization, it can be seen from Figure 4.15 that machine learning model has achieved strong correlation to training dataset where the model follows a decreasing trend with the increase of nominal stress inside the matrix and also decent with the increase in angle of orientation of major axis with principal stress direction. Hence, we have developed a model to predict stress

concentration factor inside the particle. Now, this model can be used to predict stress inside matrix as a function of stress inside particle from micro-mechanical Raman spectroscopy, particle orientation with principle stress direction, the ratio of principle stresses and geometry of the particle.

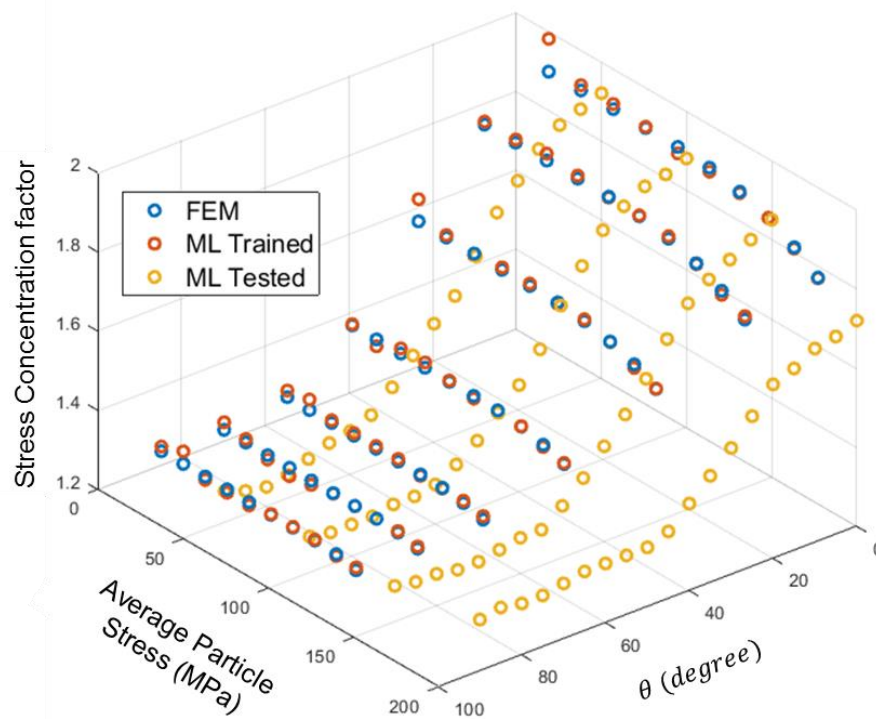


Figure 4.15 Prediction of stress concentration factor using machine learning model

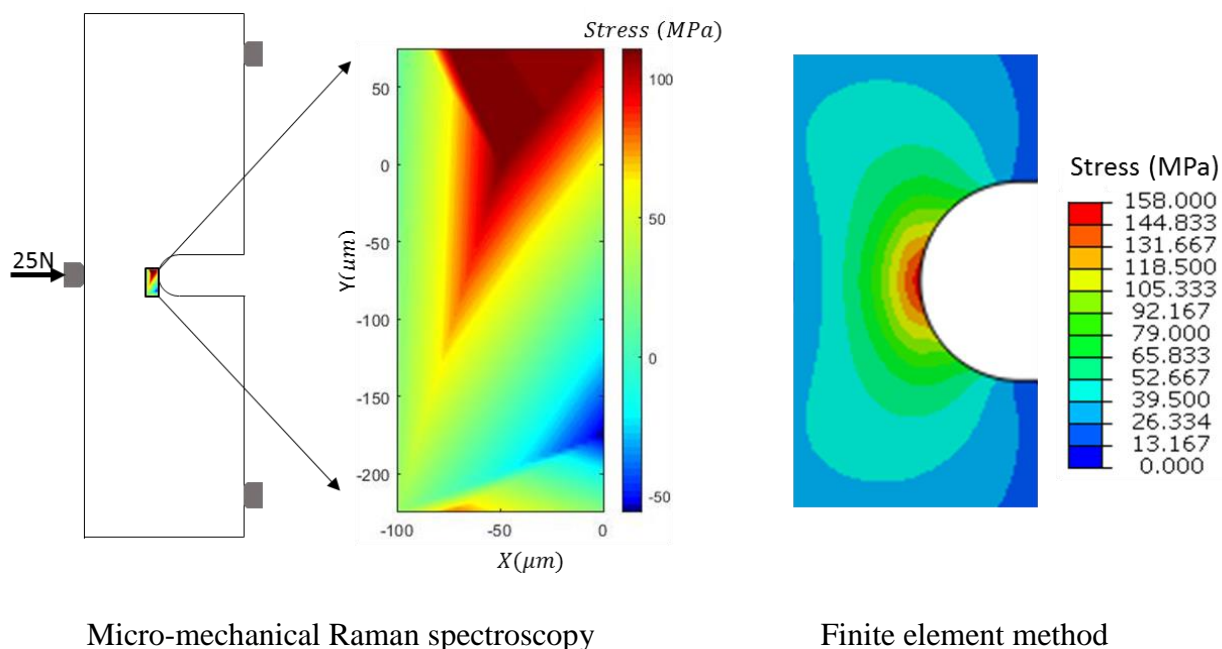


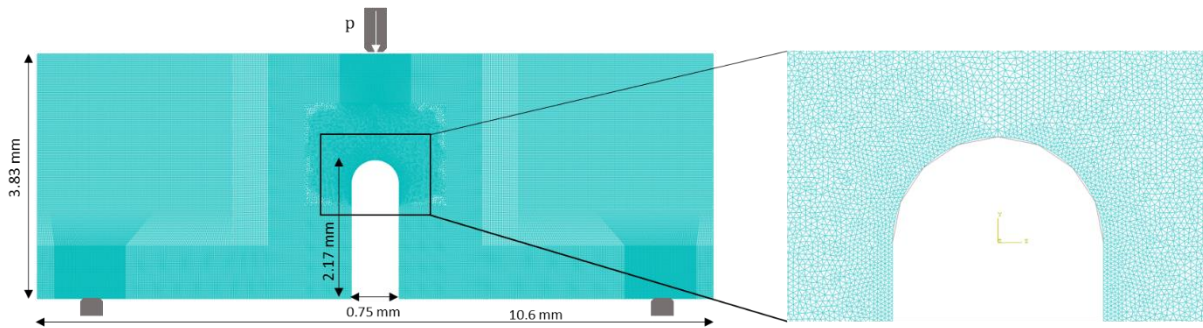
Figure 4.16 Prediction of stress distribution around the notch for stresses in non-linear elastic domain

Figure 4.16 shows the stress distribution around the notch using predicted stress from machine learning model based on stress inside particle obtained from micro-mechanical Raman spectroscopy and other variables for the case when the force of 25 N was applied by the punch. The predicted stress distribution is in accordance to the stress distribution from finite element methods where maximum stress around the notch is slightly higher than the stress predicted experimentally. It can be concluded that the model has accounted for the non-linear behavior as predicted stress around the notch are much lower than stress expected for linear elastic behavior. The method of obtaining stress distribution using finite element method is discussed below.

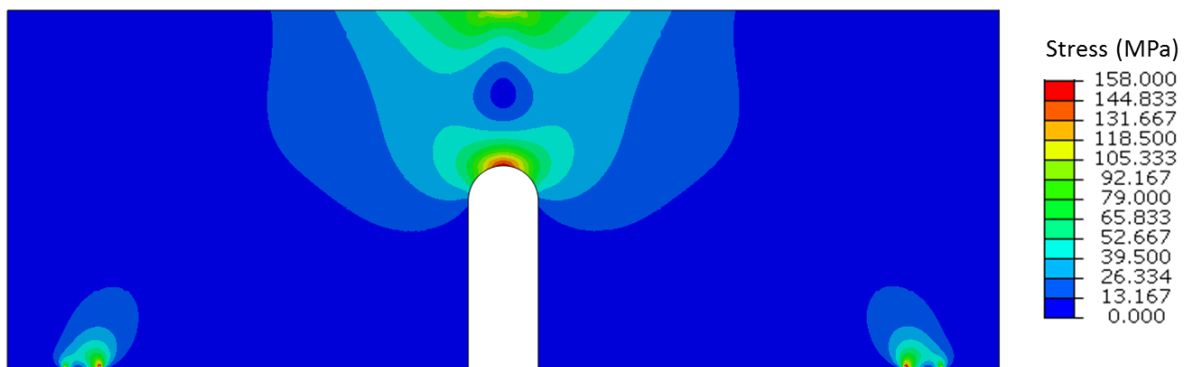
Figure 4.17 (A) shows the mesh generated for 3-point bending specimen where refined triangular mesh was generated near punch, roller and area around the notch. The load applied from punch was simulated as a distribution load of 50 N/mm applied over the length of 0.5 mm. Figure 4.17 (B) shows the stress distribution around the notch obtained from FEM and Figure 4.17 (C)

shows the convergence at 1.25 lakh elements and further mesh refining do not affect the results of finite element method.

A



B



C

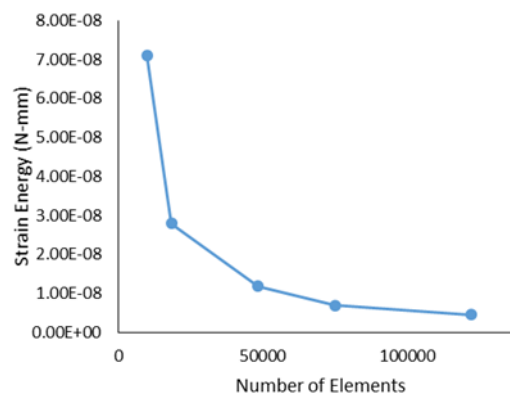


Figure 4.17 A) Mesh generated for 3-point bending specimen B) Stress distribution obtained from FEM C) Convergence of FEM model for 3-point bending test

## CHAPTER 5. SUMMARY, CONCLUSIONS, AND RECOMMENDATIONS

This work presents an innovative technique to obtain stress induced inside on a structure with non-linear material behavior (i.e. epoxy resin in this work) using micro-mechanical Raman spectroscopy. The direct stress measurements are obtained using mechanical Raman spectroscopy an imperial relationship between equivalent stress and change in Raman shift. The imperial relationship linear elastic deformation was obtained using a uniaxial compression tests. This linear relationship is not valid for large non-linear deformations. This limitation was overcome by dispersion of small amount of strontium titanate particles inside epoxy resin matrix where equivalent stress was obtained using imperial relation for change in Raman shift for particles due to stretching of epoxy resin matrix around it. The correlation between stress induced inside ceramic particles and epoxy resin matrix was obtained through pre-determined stress concentration factor. Artificial neural network was used for predicting stress concentration factor based on the geometry of the particle, orientation of the particle, stress inside ceramic particles and ratio of stresses in principle directions based on results obtained through finite element method. The mechanical characterization of epoxy resin and composite was achieved through nanoindentation experiments using spherical indenter to obtain stress-strain curve. The predicted stress values in non-linear domain accounts for the non-linear behavior of the material. However, the predicted stress around the notch is small compared to results from finite element method. This deviation can be attributed to the lack of interface behavior from finite element method. Hence, this technique can be further explored to predict stress beyond yield stress in flow stress and plastic deformation region by including further information on deformation mechanics. While extending this technique beyond yield strength of the material, the interface mechanics, particle fracture and interface delamination

has to be modeled inside finite element method to obtain correct values for stress concentration factor. Machine learning model can be improved by including experimental data for model to be biased towards experimental data.

## REFERENCES

1. Prakash, C., et al., *Effect of interface chemistry and strain rate on particle-matrix delamination in an energetic material*. Engineering Fracture Mechanics, 2018. **191**: p. 46-64.
2. Prakash, C., I.E. Gunduz, and V. Tomar, *Effect of Strain Rate and Interface Chemistry on Failure in Energetic Materials*. Fracture, Fatigue, Failure and Damage Evolution, Vol 7, 2018: p. 7-12.
3. Prakash, C., et al., *Strain rate dependent failure of interfaces examined via nanoimpact experiments*, in *Challenges in Mechanics of Time Dependent Materials, Volume 22017*, Springer. p. 93-102.
4. Verma, D., M. Exner, and V. Tomar, *An investigation into strain rate dependent constitutive properties of a sandwiched epoxy interface*. Materials & Design, 2016. **112**: p. 345-356.
5. Zhang, Y., D.P. Mohanty, and V. Tomar, *Visualizing In Situ Microstructure Dependent Crack Tip Stress Distribution in IN-617 Using Nano-mechanical Raman Spectroscopy*. Jom, 2016. **68**(11): p. 2742-2747.
6. Zhang, Y., D.P. Mohanty, and V. Tomar, *Analyses of Nanoscale to Microscale Strength and Crack-Tip Stresses Using Nanomechanical Raman Spectroscopy in IN-617*, in *Challenges in Mechanics of Time Dependent Materials, Volume 22017*, Springer. p. 9-16.
7. Zhang, Y., C. Prakash, and V. Tomar, *In-situ Crack Tip Stress Measurement at High Temperature in IN-617 Using Combined Nano-Indentation and Nano-Mechanical Raman Spectroscopy*, in *Fracture, Fatigue, Failure and Damage Evolution, Volume 62019*, Springer. p. 51-56.
8. Zhang, Y., H. Wang, and V. Tomar, *Visualizing Stress and Temperature Distribution During Elevated Temperature Deformation of IN-617 Using Nanomechanical Raman Spectroscopy*. Jom, 2018. **70**(4): p. 464-468.
9. Wu, X., et al., *Micro-Raman spectroscopy measurement of stress in silicon*. Microelectronics journal, 2007. **38**(1): p. 87-90.
10. Verma, D. and V. Tomar, *Interface Mechanical Strength and Elastic Constants Calculations via Nano Impact and Nanomechanical Raman Spectroscopy*. Fracture, Fatigue, Failure and Damage Evolution, Vol 7, 2018: p. 1-5.
11. Zhang, Y., M. Gan, and V. Tomar, *Nanomechanical Raman Spectroscopy in Biological Materials*. 2014.

12. Zhang, Y., M. Gan, and V. Tomar, *Raman thermometry based thermal conductivity measurement of bovine cortical bone as a function of compressive stress*. Journal of Nanotechnology in Engineering and Medicine, 2014. **5**(2): p. 021003.
13. Field, J. and M. Swain, *A simple predictive model for spherical indentation*. Journal of Materials Research, 1993. **8**(2): p. 297-306.
14. Hopfield, J.J., *Artificial neural networks*. IEEE Circuits and Devices Magazine, 1988. **4**(5): p. 3-10.
15. Zurada, J.M., *Introduction to artificial neural systems*. Vol. 8. 1992: West publishing company St. Paul.
16. Schalkoff, R.J., *Artificial neural networks*. Vol. 1. 1997: McGraw-Hill New York.
17. Abraham, A., *Artificial neural networks*. handbook of measuring system design, 2005.
18. Yegnanarayana, B., *Artificial neural networks* 2009: PHI Learning Pvt. Ltd.
19. Abadi, M., et al. *Tensorflow: a system for large-scale machine learning*. in *OSDI*. 2016.
20. Ganesan, S., A. Maradudin, and J. Oitmaa, *A lattice theory of morphic effects in crystals of the diamond structure*. Annals of Physics, 1970. **56**(2): p. 556-594.
21. Anastassakis, E., et al., *Effect of static uniaxial stress on the Raman spectrum of silicon*. solid state Communications, 1970. **8**(2): p. 133-138.
22. De Wolf, I., *Micro-Raman spectroscopy to study local mechanical stress in silicon integrated circuits*. Semiconductor Science and Technology, 1996. **11**(2): p. 139.
23. Gan, M., V. Samvedi, and V. Tomar, *Raman Spectroscopy-Based Investigation of Thermal Conductivity of Stressed Silicon Microcantilevers*. Journal of Thermophysics and Heat Transfer, 2015. **29**(4): p. 845-857.
24. Gan, M. and V. Tomar, *An in situ platform for the investigation of Raman shift in micro-scale silicon structures as a function of mechanical stress and temperature increase*. Review of scientific Instruments, 2014. **85**(1): p. 013902.
25. Gan, M. and V. Tomar, *Surface stress variation as a function of applied compressive stress and temperature in microscale silicon*. Journal of Applied Physics, 2014. **116**(7).
26. Gan, M., Y. Zhang, and V. Tomar, *In situ deformation of silicon cantilever under constant stress as a function of temperature*. Journal of Nanotechnology in Engineering and Medicine, 2014. **5**(2): p. 021004.
27. Mohanty, D.P., et al., *A nanomechanical Raman spectroscopy based assessment of stress distribution in irradiated and corroded SiC*. Journal of Nuclear Materials, 2017. **497**: p. 128-138.

28. Olokun, A., et al. *Interface Chemistry Dependent Mechanical Properties in Energetic Materials Using Nano-Scale Impact Experiment*. 2019. Cham: Springer International Publishing.
29. Prakash, C., et al., *Interface Mechanical Properties in Energetic Materials Using Nanoscale Impact Experiment and Nanomechanical Raman Spectroscopy*, in *Nano-Energetic Materials*, S. Bhattacharya, et al., Editors. 2019, Springer Singapore: Singapore. p. 275-290.
30. Verma, D., C. Prakash, and V. Tomar, *Interface Mechanics and its Correlation with Plasticity in Polycrystalline Metals, Polymer Composites, and Natural Materials*. *Plasticity and Impact Mechanics*, 2017. **173**: p. 1266-1274.
31. Wood, J.R., Q. Zhao, and H.D. Wagner, *Orientation of carbon nanotubes in polymers and its detection by Raman spectroscopy*. *Composites Part a-Applied Science and Manufacturing*, 2001. **32**(3-4): p. 391-399.
32. Wolf, I.D., *Stress measurements in Si microelectronics devices using Raman spectroscopy*. *Journal of Raman spectroscopy*, 1999. **30**(10): p. 877-883.
33. Kalidindi, S.R. and S. Pathak, *Determination of the effective zero-point and the extraction of spherical nanoindentation stress–strain curves*. *Acta Materialia*, 2008. **56**(14): p. 3523-3532.
34. Pathak, S. and S.R. Kalidindi, *Spherical nanoindentation stress–strain curves*. *Materials Science and Engineering: R: Reports*, 2015. **91**: p. 1-36.
35. Fischer-Cripps, A., *Use of combined elastic modulus in the analysis of depth-sensing indentation data*. *Journal of Materials Research*, 2001. **16**(11): p. 3050-3052.

## PUBLICATIONS

1. Dhiman, A., Sharma, A., Shashurin, A., and Tomar, V., *Strontium Titanate Composites for Microwave-Based Stress Sensing*, Jom, 2018: p. 1-5.
2. Li, B., Adams, R. A., Kazmi, J., Dhiman, A., Adams, T. E., Pol, V. G., & Tomar, V., *Investigation of Response of LiCoO<sub>2</sub> Cathode to Dynamic Impact Using Raman Imaging-Based Analyses*, Jom, 2018: p. 1-7.
3. Wang, H., Dhiman, A., Ostergaard, H., Zhang, Y., Siegmund, T., Kruzic, J., Tomar V., *Nanoindentation Based Properties of Inconel 718 at High Temperatures: Conventional versus Additively Manufactured*, IJP , 2018, (Submitted).
4. Park, H., Dhiman, A., Yettella, V., Tomar, V., and Zhou, Q., *In Situ Mechanical Raman Spectroscopy for Monitoring of Chlorpropamide Polymorphic Transformation during Tableting*, AAPS (2018).